JGR Atmospheres

RESEARCH ARTICLE
10.1029/2022JD036519

Satellite-Based Detection of Secondary Droplet Activation in Convective Clouds

Avichay Efraim[1], Oliver Lauer[2], Daniel Rosenfeld[1], Ramon C. Braga[3], Marco A. Franco[2,4], Leslie A. Kremper[2], Yannian Zhu[5,6], Ulrich Pöschl[2], Christopher Pöhlker[2], Meinrat O. Andreae[2,7,8], Paulo Artaxo[3], Alessandro C. de Araújo[9,10], and Mira L. Pöhlker[2,9,11]

[1]Institute of Earth Sciences, The Hebrew University of Jerusalem, Jerusalem, Israel, [2]Multiphase Chemistry Department, Max Planck Institute for Chemistry, Mainz, Germany, [3]National Marine Science Centre, Southern Cross University, Coffs Harbour, Australia, [4]Institute of Physics, University of São Paulo, São Paulo, Brazil, [5]School of Atmospheric Sciences, Nanjing University, Nanjing, China, [6]Joint International Research Laboratory of Atmospheric and Earth System Sciences & Institute for Climate and Global Change Research, Nanjing University, Nanjing, China, [7]Department of Geology and Geophysics, King Saud University, Riyadh, Saudi Arabia, [8]Scripps Institution of Oceanography, UCSD, La Jolla, CA, USA, [9]Faculty of Physics and Earth Sciences, Leipzig Institute for Meteorology, University of Leipzig, Leipzig, Germany, [10]Brazilian Agricultural Research Corporation (EMBRAPA), Belém, Brazil, [11]Experimental Aerosol and Cloud Microphysics Department, Leibniz Institute for Tropospheric Research, Leipzig, Germany

Abstract We present a new approach of analyzing and interpreting vertical profiles of cloud microstructure obtained by satellite remote sensing. The method is based on a spectral bin microphysics adiabatic parcel model and aims to elucidate the effects of aerosols on the evolution of convective clouds and related microphysical processes, including the activation of cloud condensation nuclei (CCN), the growth of cloud droplets, and the formation of precipitation. Characteristic features in the vertical profiles of effective radius (r_e) and temperature (T) reveal different microphysical zones in convective clouds related to the change increase of r_e with decreasing T. The classification of the different microphysical zones includes the (a) condensational growth of droplets, (b) growth by coalescence, (c) rainout, (d) secondary droplet activation zone (SAZ), (e) mixed-phase of ice particles and water droplets, and (f) glaciation of the cloud. The detection of the SAZ is introduced here for the first time. This method allows us to identify the activation of aerosol particles above cloud base and their role in the invigoration of deep convective clouds.

Plain Language Summary Using satellite remote sensing, we can obtain the vertical profiles of cloud microphysical processes in developed clouds. In this study, we present a new way of analyzing these profiles and understand the different processes that cloud droplets undergo during the development of the cloud. These processes include the turning of aerosols into cloud droplets, and the droplets' coalescence into rain drops. The change of droplets' size with height, as obtained by the satellite, reflect the different microphysical processes inside the cloud. While expecting the droplets to grow with height, a decrease of the droplets size suggests either rainout of the larger droplets from the cloud; or creation of small new droplets at much greater heights than the cloud base, where they are usually created. Those processes can be related to the extent of decrease of cloud drop size with height. The detection of new droplet formation above the cloud base with satellite is introduced here for the first time and it allows to understand this microphysical process and its effect of the development of the clouds and precipitation.

Key Points:

- A new method to interpret the cloud microstructure of deep convective clouds from satellite remote sensing is presented in this study
- The microphysical process of secondary activation of droplets above cloud bases is demonstrated with a model and detected in observations
- The satellite detection of the secondary activation microphysical zone is introduced here for the first time

Supporting Information:

Supporting Information may be found in the online version of this article.

Correspondence to:

A. Efraim and M. L. Pöhlker,
Avichay.Efraim@mail.huji.ac.il;
m.pohlker@mpic.de

Citation:

Efraim, A., Lauer, O., Rosenfeld, D., Braga, R. C., Franco, M. A., Kremper, L. A., et al. (2022). Satellite-based detection of secondary droplet activation in convective clouds. *Journal of Geophysical Research: Atmospheres*, *127*, e2022JD036519. https://doi.org/10.1029/2022JD036519

Received 19 JAN 2022
Accepted 28 MAY 2022

Author Contributions:

Conceptualization: Avichay Efraim, Oliver Lauer, Daniel Rosenfeld, Mira L. Pöhlker
Formal analysis: Avichay Efraim, Oliver Lauer
Investigation: Avichay Efraim, Oliver Lauer
Methodology: Avichay Efraim, Oliver Lauer, Daniel Rosenfeld, Ramon C. Braga, Marco A. Franco, Leslie A. Kremper, Yannian Zhu
Resources: Avichay Efraim, Ramon C. Braga, Marco A. Franco, Leslie A. Kremper, Alessandro C. de Araújo, Mira L. Pöhlker

1. Introduction

1.1. Background

The effects of aerosols on clouds and climate are among the largest uncertainties in the assessment and modeling of climate change (IPCC, 2013, 2021). The investigation of aerosols and clouds using remote sensing techniques allows global monitoring and analysis of aerosol-cloud interactions (e.g., Bréon et al., 2002; Grosvenor et al., 2018; Rosenfeld et al., 2016; Rosenfeld and Lensky, 1998). A main challenge, however, is to investigate aerosol and cloud properties at an accuracy that suffices to quantify the response of cloud microstructure and the corresponding radiative effects to aerosol perturbations. Aerosols serving as cloud condensation nuclei (CCN) determine the droplet number concentration (N_d) at cloud base for a given cloud base updraft speed (w_b), and

Software: Avichay Efraim, Oliver Lauer, Yannian Zhu
Supervision: Daniel Rosenfeld, Mira L. Pöhlker
Visualization: Avichay Efraim
Writing – original draft: Avichay Efraim, Oliver Lauer
Writing – review & editing: Avichay Efraim, Oliver Lauer, Daniel Rosenfeld, Ramon C. Braga, Marco A. Franco, Leslie A. Kremper, Yannian Zhu, Ulrich Pöschl, Christopher Pöhlker, Meinrat O. Andreae, Paulo Artaxo, Mira L. Pöhlker

subsequently dominate the cloud microphysical and precipitation processes. The impact of fine ($d < 1$ μm) and ultrafine ($d < 0.1$ μm) aerosol particles (UAP) on deep convective clouds can be substantial through the following two mechanisms:

1. Suppression of warm rain: For a given updraft speed, polluted conditions with high CCN number concentrations (N_{CCN}) lead to the formation of clouds with high N_d and small r_e at cloud base (Twomey, 1977). In such conditions, collision and coalescence processes are inhibited, thus delaying the droplets' growth into rain drops (Gunn and Phillips, 1957; Squires, 1958). Hence, extra latent heat is caused by the air parcels' ability to hold more liquid water content (LWC). This increases the updraft speed and maintains the clouds at a higher altitude. When postponing the rain initiation while the cloud continues to grow vertically, the cloud droplets are transported to above the zero-isotherm and freeze into ice hydrometeors (Braga et al., 2017). As a result, latent heat of freezing is released and increases the buoyancy, causing an invigoration of the cloud toward the tropopause, where it spreads aside into wide anvils (Rosenfeld, Lohmann, et al., 2008).
2. Invigoration by activation of droplets above cloud base: This is typically found in clean air masses with relatively low N_{CCN}, which result in large r_e and a corresponding high coalescence efficiency. The drop coalescence reduces the integrated droplets' surface area, which reduces the condensation rate. As a result, the supersaturation (S) increases to the point where it exceeds the S at cloud base allowing activation of CCN with high critical S (typically UAP) that were not activated at cloud base. The activation of particles into cloud droplets high above the cloud base releases additional latent heat, increases the buoyancy, and invigorates the clouds (Fan et al., 2018; Khain et al., 2012).

The invigoration caused by these mechanisms creates larger and colder anvils (Fan et al., 2013; Pan et al., 2021), which may emit less longwave radiation to space and thus creates a positive radiative forcing and warms the Earth (Cotton et al., 2011; Slingo & Slingo, 1988). In addition, the evaporation of tiny ice crystals from these high anvils is likely to enrich the upper troposphere with water vapor, which is a strong greenhouse gas and thus likely to increase the positive radiative forcing.

Aerosol optical depth (AOD) has been extensively used as a proxy for N_{CCN} (Feingold et al., 2001; Quaas et al., 2009). The Aerosol Index (AI), which is the product of AOD and Angström exponent (Nakajima et al., 2001), provides a better estimation for N_{CCN}. However, Shinozuka et al. (2015), showed that such optically retrieved N_{CCN} could vary by an order of magnitude compared to the directly measured N_{CCN}. Furthermore, the satellite-retrieved AOD and AI become insensitive to $N_{CCN} < 150$ cm^{-3} due to the small signal-to-noise ratio. This threshold varies greatly depending on the size of the CCN and their activation supersaturation (Shinozuka et al., 2015).

The N_d can also be retrieved based on the vertical evolution of r_e in the growing convective towers. This approach relies on the remarkable aircraft observations, which show that r_e increases with height above cloud base almost as if the clouds were adiabatic, despite the fact that the cloud LWC is mostly smaller than adiabatic (Freud et al., 2011). This pattern is caused by the nearly inhomogeneous mixing behavior of the convective clouds with the ambient air. Based on in-cloud aircraft measurements, Freud et al. (2011) showed that the cloud base N_d could be approximated by dividing the adiabatic LWC by the mass of a single droplet having an adiabatic r_e. Since both, r_e and cloud top temperature, can be retrieved by satellites, N_d could be calculated based on the assumption of adiabatic r_e and LWC (Rosenfeld, Fischman, et al., 2014; Rosenfeld, Liu, et al., 2014). The adiabatic LWC as a function of temperature can be calculated based on the retrieved cloud base temperature and pressure (Freud et al., 2011). The knowledge of the cloud base height above the surface, H_b, also allows estimating w_b, which can be obtained as $w_b = 0.9H_b$, with H_b in km, and w_b in ms^{-1} (Zheng and Rosenfeld, 2015). The cloud base maximum S (S_{max}) can be calculated based on N_d and w_b (Pinsky et al., 2012). The N_d is then by definition $N_{CCN}(S)$. All these considerations were combined by Rosenfeld et al. (2016) into a satellite methodology to retrieve cloud base N_d and S, which further yields $N_{CCN}(S)$ with an accuracy of ±30%.

However, N_d and N_{CCN} can be retrieved from vertical T-r_e profiles only as long as condensation dominates the cloud droplets' growth (i.e., for $r_e < 14$ μm). Drop coalescence increases dr_e/dT beyond the condensational growth rate. Rosenfeld and Lensky (1998) provided a conceptual model of the vertical evolution of T-r_e in deep convective clouds. They hypothesized that a stabilization or moderation of r_e, that is, $dr_e/dT \approx 0$, after exceeding a threshold of approximately 14 μm was considered as resulting from rainout of the larger drops from the cloud. The appearance of ice particles increases the r_e further because ice particles are typically much larger than

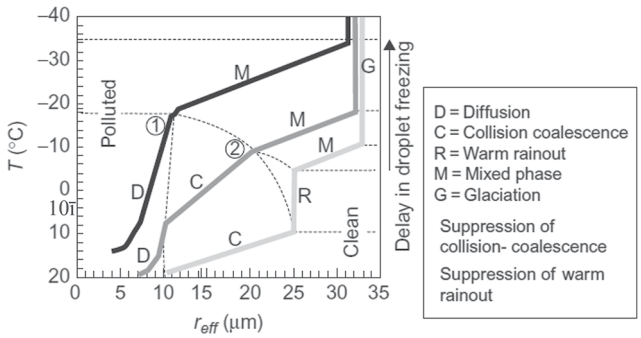

Figure 1. Conceptual diagram of the microphysical zones in convective clouds based on the vertical evolution of the T-r_e relationships as developed in (Rosenfeld & Lensky, 1998), here adopted from (Rosenfeld, 2018).

water drops in the same mixed-phase clouds. Eventually the cloud reaches a full glaciation, where the indicated r_e reaches a maximum. Rosenfeld and Lensky (1998) used the T-r_e profile to partition the clouds into five vertical microphysical zones as shown in Figure 1: (a) Diffusion and condensational growth (in short "condensation"); (b) coalescence growth; (c) rainout; (d) mixed phase; (e) glaciated cloud.

1.2. Secondary Activation Zone

The T-r_e conceptual model from Rosenfeld and Lensky (1998) in Figure 1, is based on the assumption of CCN activation into cloud droplets at cloud base. It does not consider the new activation of droplets in the course of cloud growth. The activation of particles into cloud droplets high above cloud base is referred to as secondary activation, as opposed to the primary activation of droplets at cloud base. Secondary activation can occur above cloud base in two ways: (a) The droplet coalescence reduces the integrated droplets' surface area available for condensation, which reduces the condensation rate. As a result, S might exceed the S_{max} at cloud base allowing inactivated UAP from the cloud base to nucleate into cloud droplets; (b) Additional entrained particles from the lateral and/or top boundaries of the cloud that can be activated even at the existing S at that level. Both ways will result in a reduction of the observed r_e with decreasing T due to the nucleation of small new droplets in the environment of coalesced droplets. This has been validated with several in-cloud penetration aircraft campaigns (Bera et al., 2022; Braga et al., 2017; Paluch and Baumgardner, 1989; Paluch and Knight, 1984; Prabha et al., 2011; Warner, 1969). The vertical microphysical zone where these processes occur is defined here as the "secondary activation zone" (SAZ). Clouds with enough latent heat left after warm rainout to keep the air parcel rising and which include a sufficient number of CCN can form a SAZ. The new droplets' formation releases enough latent heat to keep the cloud growing, increasing its longevity and height.

In this study, we describe an updated method to identify the microphysical zones of convective clouds based on T-r_e profiles, taking the SAZ into account. We used a spectral bin microphysics adiabatic parcel model to simulate the N_d, S, and the rain water fraction (RWF) profiles for four aerosol size distribution (ASD) and aerosol number concentrations below cloud base. The ASD and the simulated cloud properties are described in Section 3.1. Then, an application of the modeled cloud properties and their effect on the shape of the T-r_e profile is described in Section 3.2, and the effect of real measured ASD on two satellite retrieved T-r_e case studies is described in Section 3.3.

2. Methods

2.1. Model Description

In this study, we used an adiabatic cloud parcel model to describe the properties of convective clouds. The modeling was possible due to the inherent characteristic of r_e in convective clouds caused by the inhomogeneous nature of turbulent mixing at the cloud edges (Rosenfeld et al., 2016). The model is a spectral bin adiabatic parcel model developed by Pinsky and Khain (2002). This parcel model explicitly describes the cloud particle spectrum evolution using a moving mass grid containing 2000 mass bins, allowing effects on droplet collisions. The model describes the processes of aerosol particle growth, particle activation into cloud droplets, the vertical evolution of the cloud microstructure and precipitation-forming processes in the water phase ($T > -10$°C). The aerosol particles are considered as spherical NaCl particles to ensure compatibility with the model construction. The effect of different chemical compositions and hygroscopicity on cloud microphysics and ASD is beyond the scope of this study and has been addressed instead in Braga et al. (2021) and Pöhlker et al. (2021). Braga et al. (2017) have shown that the vertical evolution of the r_e measured by cloud probes generally agrees well with the theoretical r_e driven by the adiabatic growth of droplets through water condensation. When r_e exceeds 14 μm, coagulation and coalescence processes start to dominate. The coagulation process of cloud drops is calculated as proposed by Pinsky et al. (2001), who describe this process by solving stochastic collision equations according to Bott (1997). The coagulation of droplets is calculated after the initial condensational growth of particles. The drop-drop collision efficiency is calculated for each set of droplet masses allocated to the same parcel. Although

the model is very detailed, and strives to describe the basic physical processes, by considering only basic cloud properties while simplifying or ignoring additional environmental factors, the resulting microphysical processes may vary from real cloud behavior. This is discussed in Section 4.

2.2. Satellite T-r_e Retrieval

The satellite retrievals of cloud properties for the case studies described in this study were performed using the Visible Infrared Imaging Radiometer Suite (VIIRS) passive sensor, onboard the Suomi National Polar-orbiting Partnership (NPP) satellite. The VIIRS sensor has a very high spatial resolution of 375 m at the nadir in five optical channels for detailed spectral information (Rosenfeld, Fischman, et al., 2014; Rosenfeld, Liu, et al., 2014). High spatial resolution is required to resolve the vertical structure of convective clouds. At lower resolution only the largest individual convective clouds can be resolved, thus missing the fine structure required to detect the SAZ. A snapshot of the T-r_e profile of a cloud cluster provides the same information as obtained by tracking a single convective cloud throughout its vertical evolution (Arakawa and Schubert., 1974; Lensky and Rosenfeld, 2006). It is also assumed that r_e in the cloud top pixel has the same value as in more developed clouds at the same height, as long as precipitation does not fall through that level (Freud et al., 2008; Rosenfeld and Lensky, 1998). These assumptions enable to infer vertical T-r_e development of clouds in a two-dimensional spatial image. Moreover, to reduce the data distortion, the satellite zenith angle of the clouds has to be between 30° and −20°, and the solar zenith angle of the clouds has to be below 65°. The wavelengths used to retrieve the T-r_e profile include 3.7 and 10.8 μm (Rosenfeld, Fischman, et al., 2014; Rosenfeld, Liu, et al., 2014). This method assumes retrieval of water drops. However, ice particles are much larger than the droplets in the clouds, in which they are formed. They absorb more strongly the solar radiation at the 3.7 μm band. Thus, the satellite retrieved r_e of ice particles appear larger than the same size water drops. Therefore, a very large r_e at supercooled temperature usually indicates the existence of ice in the cloud.

A designated software produces an RGB display that highlights the cloud microphysics and T and r_e retrievals in each pixel. On the basis of this display, cloud scenes of interest are manually sampled to avoid or minimize obstruction by multilayer or semi-transparent clouds that can disrupt the retrieved T-r_e. A cloud mask algorithm, introduced by Zhu et al. (2014), filters out the partially filled cloudy pixels due to measurement errors in such pixels. The specific r_e values for each pixel are sorted by the detected temperature for each pixel into 1°C sized bins (i.e., 9.5–10.5°C in the 10°C bin etc.). Then, the 30-percentile median for all r_e values within one bin is calculated resulting in a continuous vertical cloud profile of r_e as a function of T (Rosenfeld et al., 2016). The effect of aerosols on the T-r_e profile is mostly reflects in the growing clouds, rather than mature dissipating clouds. Thus, the use of the 30-percentile median is meant to capture the clouds in their growing phase (Lensky and Rosenfeld, 2006; Rosenfeld, Woodley, et al., 2008). Multilayer clouds are identified by a lack of continuity in the T-r_e profiles. Therefore, this methodology is not valid for non-convective clouds or scenes obscured by multilayer clouds. The uncertainties of satellite-retrieved r_e and T are approximately 8% and 0.2–1.1°C, respectively (Rosenfeld et al., 2016). Although, the importance of those uncertainties is reduced because the method described in this study is examining the relative change of r_e with T and not the absolute values. T-r_e profiles retrieved in various locations show similar results for similar environments (e.g., Huang et al., 2022; Lensky and Rosenfeld, 2006; Rosenfeld, 2007; Rosenfeld, Woodley, et al., 2008) implying the robustness of T-r_e retrievals and the fact that this method can be applied worldwide, in any meteorology and for any convective clouds as long as a valid unperturbed T-r_e profile is retrieved. This study analyzes the satellite retrieved T-r_e profiles by an automatic algorithm to detect the different microphysical zones. The entire description of the algorithm is described in Section 3.2.

2.3. Aerosol Observations at the Amazon Tall Tower Observatory

The Amazon Tall Tower Observatory (ATTO, 2020) is located in the central Amazon Basin (2.145°S, 59.004°W at 130 m above sea level). It monitors fundamental climatic and atmospheric parameters in a vast region of pristine rainforest. Some of the meteorological measurements at ATTO include temperatures, wind profiles, and precipitation (Andreae et al., 2015). These parameters were used to determine the coupling state of the clouds scenes and to choose case studies where the air parcel that was sampled at ATTO fed the cloud that was sampled by the satellite. For each of the case studies described in Section 3.3, an ASD was measured by a Scanning Mobility Particle Sizer (SMPS, TSI Inc.) connected to an inlet line with 60 m height at an 80 m tall mast (Franco et al., 2022). An overview of the atmospheric, geographic, and ecological conditions, as well as

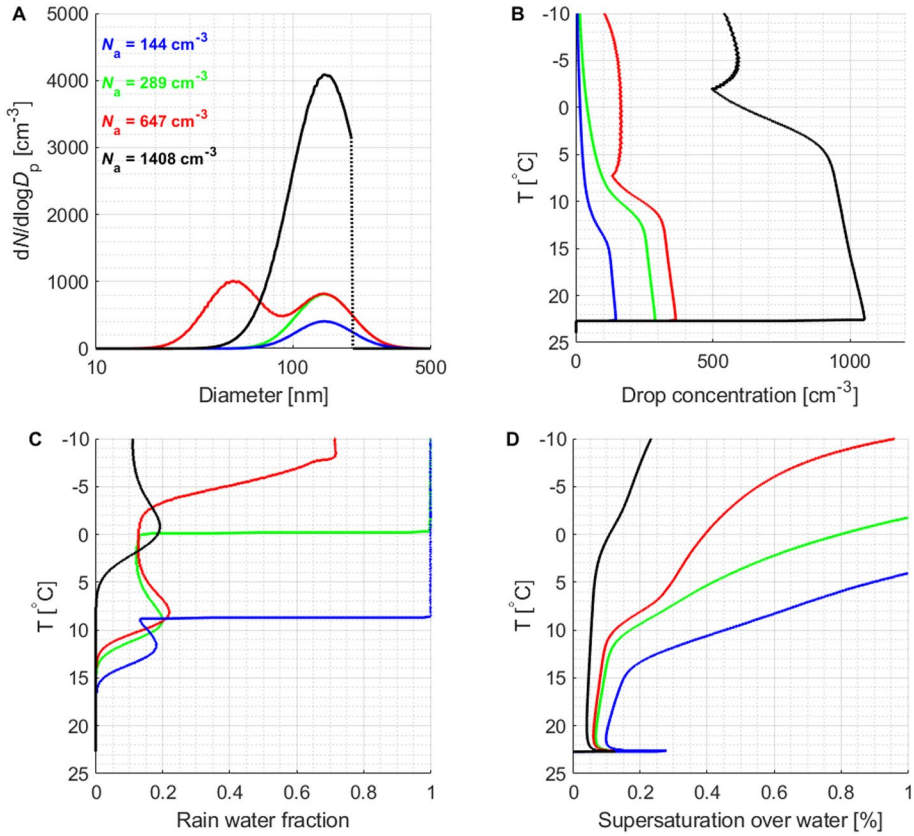

Figure 2. Simulations of cloud properties for four different aerosol size distributions (ASD) and total particle number concentrations (N_a). Panel A shows the four ASD including the cases (1) very clean unimodal (blue) with N_a = 144 cm^{-3}, monomodal size distribution, with accumulation mode only; (2) clean unimodal (green) with N_a = 289 cm^{-3}, monomodal size distribution, with accumulation mode only; (3) clean bimodal (red) with N_a = 647 cm^{-3}, bimodal size distribution, the same number of accumulation mode particles as clean unimodal and additional Aitken mode particles; (4) polluted (black) with N_a = 1,408 cm^{-3}, wide monomodal size distribution, with mostly accumulation mode reaching into the Aitken mode. The polluted ASD is truncated at 200 nm to prevent early warm rain initiation by enhanced coalescence. Panel B shows the simulated N_d with decreasing T. Panel C shows the vertical rain water fraction (RWF) profile. RWF is defined as the ratio between rain water content to total water content, where drops with a diameter >50 μm are considered raindrops. Due to the lack of significant activation of new droplet in the very clean unimodal and clean unimodal cases (shown in Figure 3), RWF jumps to unity when the smallest drops grow beyond the threshold of 50 μm. In reality, the drop size distribution is wider, and therefore, there would not be such a sharp jump. In addition, clouds that completely rainout cannot develop due to a lack of condensation and buoyancy. The model forces the cloud to grow beyond this point in order to compare clouds profiles with and without significant new activation. Panel D shows the vertical profile of supersaturation over water.

commonly encountered air masses, can be found, for example, in Artaxo et al. (2013), Andreae et al. (2015), and Pöhlker et al. (2019). Characteristic aerosol and CCN conditions at ATTO have been described in recent studies (e.g., Moran-Zuloaga et al., 2018; Pöhlker et al., 2016, 2018).

3. Results

3.1. Simulations of Cloud Microphysical Properties

This section discusses the vertical T-r_e profiles of convective clouds using the parcel model with various initialization values. The simulations were performed for four ASD measured in subsaturated conditions (Braga et al., 2021; Pöhlker et al., 2021) as shown in Figure 2a. The data and initial thermodynamic conditions for the simulations, such as pressure, temperature, relative humidity, and height were collected below cloud bases of convective clouds during flight AC19 of the ACRIDICON-CHUVA campaign (Wendisch et al., 2016). The ASD include three monomodal ASD and one bimodal ASD that simulates a Hoppel minimum. The Hoppel minimum is a size separation gap between two size modes, which usually indicates the size of the smallest particles that can

serve as CCN for the given thermodynamical conditions due to cloud processing (Hoppel and Frick, 1986; Hudson et al., 2015). The two size modes are the Aitken mode, with particles smaller than the Hoppel minimum (from approximately 10 to 70 nm), and the accumulation mode, which includes the larger ones (from approximately 70 to 200 nm) (Seinfeld and Pandis, 1998). The three monomodal ASD have only an accumulation mode for different aerosol number concentrations (cases: very clean unimodal, clean unimodal, and polluted) and the bimodal ASD has Aitken and accumulation modes (case: clean bimodal). Even though observations show no warm rain for similarly polluted cases (Braga et al., 2017), the model still simulates rain due to its construction. Therefore, to prevent or at least delay the initiation of warm rain by nucleation of large droplets and enhanced coalescence, the polluted ASD is truncated at 200 nm and lacks particles larger than this threshold. The comparison of the polluted ASD with and without the truncation is illustrated in the supplements (Figure S1). The increase of updraft speed with height is assumed to be linear with a constant acceleration of 0.9 ms^{-1} km^{-1}. These are typical velocities found near the base of convective clouds (Zheng and Rosenfeld, 2015). The aerosol spectra and the respective vertical profiles of cloud properties for each ASD case are presented in Figure 2, the droplet size distribution (DSD) for each T bin is presented in Figure 3 and the corresponding T-r_e profiles from the model runs are shown in Figure 4.

The number of activated drops at cloud base is mostly influenced by accumulation mode particles, which are activated first (Pöhlker et al., 2016, 2018). As can be seen in Figure 2b, N_d at cloud base is almost equal to the N_a for the very clean unimodal and clean unimodal cases, while for the clean bimodal and polluted cases, N_d at cloud base is much smaller than the total N_a, meaning that a large fraction of the particles was not activated at cloud base. The inactivated particles are activated aloft when S exceeds S_{max} at a higher altitude (Figure 2d). Figure 3 shows the DSD in each T bin, colored by the number concentration of each size bin. For all four ASDs an increase of droplet concentration appears above the cloud base. However, the number concertation of activated droplets above cloud base in the very clean unimodal and clean unimodal cases is of at least two orders of magnitude lower than in the clean bimodal and polluted cases. The ratio of the number of activated droplets with respect to the number of eliminated large drops in the clean bimodal and polluted cases is much larger, which means a much more significant SAZ. This is noticeable in the increasing drop concentration with decreasing T for those cases (Figure 2b). In addition, Figure 3 shows the conversion of cloud droplets into raindrops which populate the larger size bins.

RWF is defined as the ratio between the rain water content ($d > 50$ μm) and the total water content (Figure 2c). RWF starts to increase as coalescence start and to decrease as the rain drops precipitate from the cloud parcel. This process takes place when the terminal velocity of raindrops is larger than the updraft speed within the cloud parcel. When the SAZ is negligible (very clean unimodal and clean unimodal cases) RWF increases with decreasing T up to unity when the smallest drops grow beyond the threshold of 50 μm. In reality, the drop size distribution would be wider, and therefore, there would not be such a sharp jump. In addition, clouds that completely rain out cannot develop higher due to a lack of condensation and buoyancy. In this study, the model forces the cloud to grow beyond this point to illustrate how secondary activation changes the T-r_e profile compared to the alternative that is rarely realized in nature. The height for the onset of rain formation above the cloud base (RWF > 0) increases for increasing N_d at cloud base (Figures 2c and 3). This is consistent with the delayed coalescence at greater N_d due to slower droplet growth with height. The N_d starts to decrease sharply at the temperature of rain initiation, as the coalescence merges many cloud droplets into fewer raindrops. For simulations in which N_d starts to increase above cloud base (clean bimodal and polluted) the existence of a significant SAZ is identified. This occurs at the height where S exceeds the S_{max} at the cloud base. In these cases, a considerable amount of aerosol particles that were not activated into droplets near the cloud base are activated at the larger S aloft. This is valid for these model runs since the model does not include entrainment of additional aerosol particles. However, in nature, the origin of these particles is not necessarily inactivated aerosols from the cloud base, but they could also be from the surroundings, for which S does not have to exceed S_{max}. The significant activation of the new droplets in these cases replenishes the cloud water content; therefore, RWF values do not go up to 1.

3.2. Detection of Microphysical Zones Based on Modeled T-r_e Profiles

Different microphysical processes determine the shape of the T-r_e profiles of convective clouds. These processes were investigated using the model results described in Section 3.1. Figure 4 shows the T-r_e profiles of the four simulated clouds with varying shapes and colors representing the different microphysical zones. The gray lines in the background of the plot are the theoretical adiabatic r_e curves under the assumption of condensational growth for different cloud base N_d. The adiabatic curves are calculated based on the adiabatic LWC and the correspond-

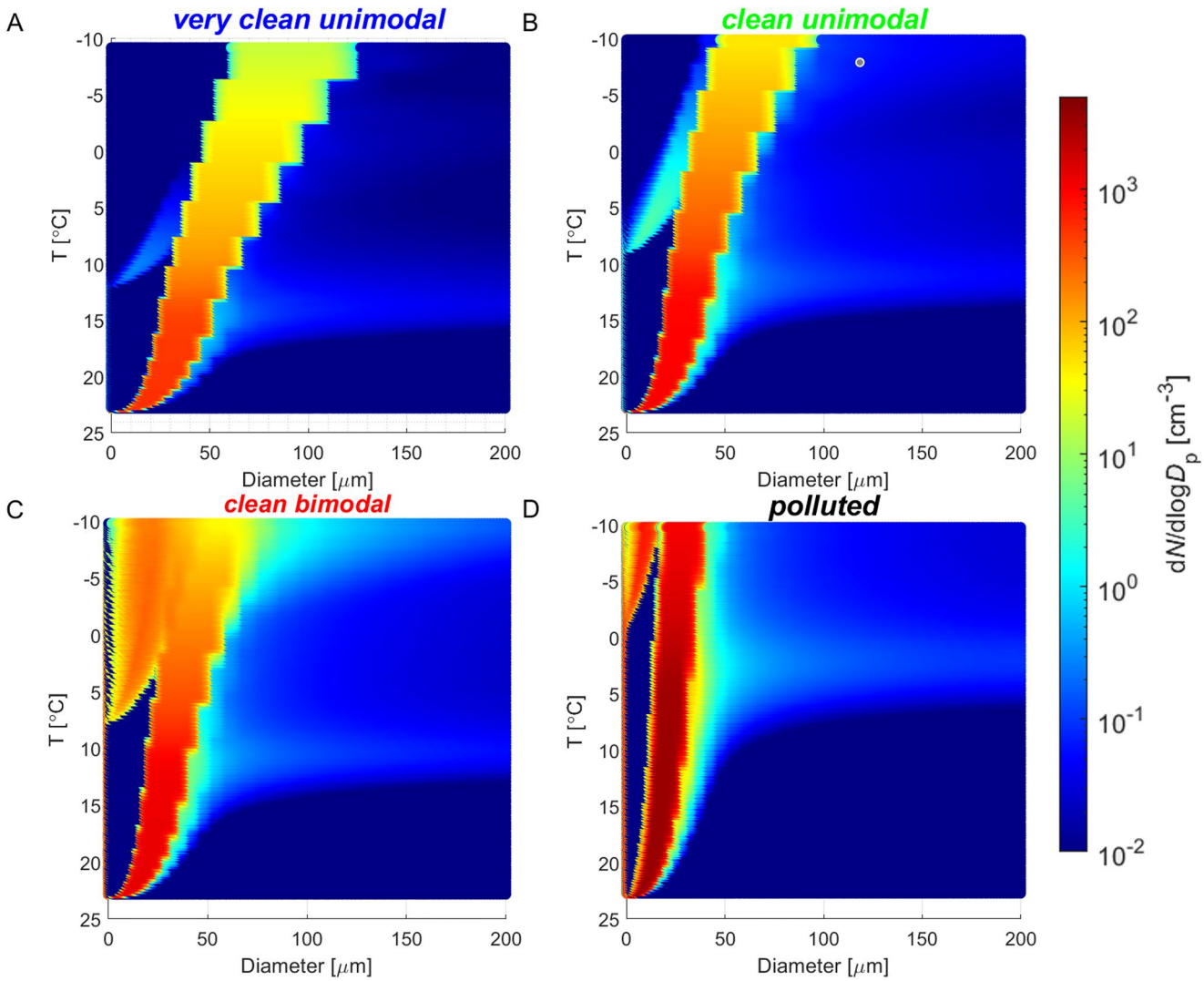

Figure 3. The droplet size distribution (DSD) in each T bin, colored by the number concentration of each size bin, for the four model runs presented in Figure 2. It is inferred from this figure that SAZ occurs in all four ASD. However, in Panel A and B (very clean unimodal and clean unimodal cases) the number concentration of activated droplets above cloud base is at least two orders of magnitude lower than the clean bimodal and polluted cases shown in panels C and D. Therefore, the ratio of droplets activation to large drops elimination in the clean bimodal and polluted cases is larger, which means a much more significant SAZ. This causes an increase in drop concentration with deceasing T (Figure 2b). It is also shown here that the rain initiation is higher for cases with higher initial N_d.

ing development of r_e. The adiabatic LWC is computed using an adiabatic parcel model that rises from the cloud base temperature and pressure obtained from reanalysis (Rosenfeld et al., 2016). The deviations between the actual and the theoretic adiabatic T-r_e profiles define the dominant microphysical zones, as follows:

1. **Condensation:** The first zone after droplets nucleation at cloud base (red lines in Figure 4). The r_e growth is similar to an adiabatic r_e curve originating at cloud base. Therefore, the T-r_e line is nearly parallel to the background T-r_e curve with the same cloud base N_d. During the condensational growth phase, no rain is expected, and thus, no rain was modeled.
2. **Adiabatic growth:** There are cases where the T-r_e growth continues adiabatically well beyond the r_e threshold of rain initiation, which is commonly recognized near 14 μm (e.g., Rosenfeld et al., 2006). Beyond this threshold, the microphysical zone can no longer be defined as dominantly condensational since coalescence has become very efficient and likely plays a significant role here as well. Accordingly, the continuation of the adiabatic increase in r_e beyond 14 μm is defined as adiabatic growth here (orange lines in Figure 4) to be differentiated from the condensational growth. Such behavior may result from strong updrafts, where there is not enough time to form rain in the fast-rising parcels.

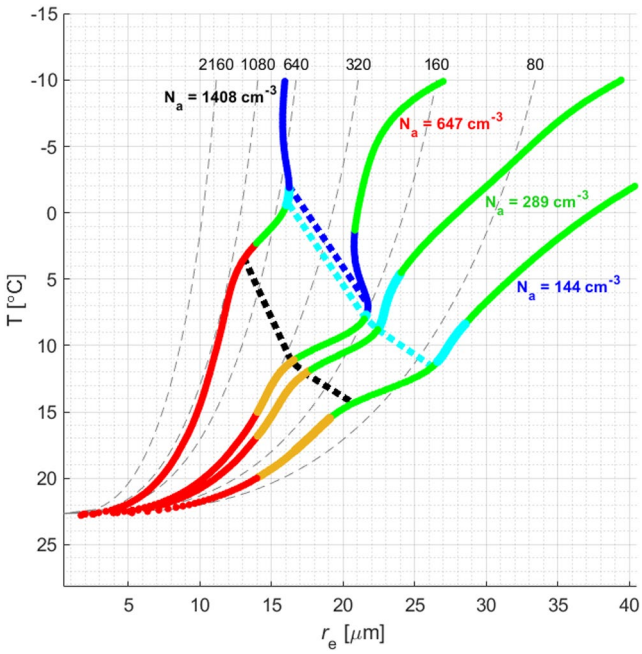

Figure 4. T-r_e profiles of the four cloud simulations presented Figure 2, color-coded by different microphysical zones based on the growth rate of r_e with decreasing T. The thin gray dashed lines in the background are the theoretical adiabatic curves. The red lines are the condensational growth phase. The orange lines mark the adiabatic growth. The green lines mark the coalescence growth. The cyan lines mark the rainout, and the blue lines mark the secondary activation zone (SAZ). The thick dashed black, cyan and blue lines indicate the rain onset, maximum rainout, and the SAZ onset, respectively.

3. **Coalescence:** Drop coalescence increases the cloud drop size due to the drops merging. Therefore, a growth rate of r_e that exceeds the adiabatic growth rate marks the coalescence zone (green lines in Figure 4). The model shows the initiation of rain (Figure 2c) at the bottom of the coalescence zone. Consequently, N_d sharply reduces.
4. **Rainout:** Moderation of the growth rate of r_e with decreasing T above the coalescence zone indicates rainout of the larger raindrops from the cloud parcel/top (cyan lines in Figure 4).
5. **Secondary activation zone:** A significant activation of new droplets after the occurrence of coalescence and/or rainout is indicated by negative dr_e/dT (blue lines in Figure 4).

Figure 4 shows that the microphysical zones are distinguished from each other by the shape of the T-r_e profiles. In all the four cloud simulations, the condensational part of the cloud (marked by red lines) behaves adiabatically and follows the theoretical adiabatic curves, depending on the N_a of each case. Then, the coalescence that comes after the adiabatic part indicates the cloud droplets' transition to raindrops. The depth of rain initiation (D_r, in meters above cloud base) is linearly correlated with N_d at cloud base, according to $D_r \sim 4 \cdot N_d$ (Freud & Rosenfeld, 2012; Konwar et al., 2012). For example, in the very clean unimodal case, r_e increases fastest with decreasing T and reaches rain initiation at the warmest T. The maximum conversion rate of cloud into raindrops (maximum rainout, marked by the thick cyan dashed line) occurs at approximately 12°C. For cases with higher initial N_d, the temperature of rain initiation (marked by the dashed black line) and maximum rainout occur at colder temperatures (see Figures 2–4). Coalescence and precipitation lead to a strong reduction in the droplets' integrated surface area, causing limitations to the condensation rate. This increases S with decreasing T. In the clean and very clean unimodal cases, which have an accumulation mode only, all the aerosols get activated at cloud base, as seen in Figure 2b. The cloud droplets are larger, and their precipitation causes only a slight decrease of dr_e/dT, which remains positive. However, in the clean bimodal and polluted cases, the significant amount of Aitken mode particles that were not activated at cloud base get activated above cloud base because of the increase of S beyond S_{max} at cloud base. This results in a decrease of r_e with decreasing T (SAZ, marked by the blue lines). Such a pattern is observed due to the relative increase of the newly activated small droplet concentrations in the cloud parcel. This signature in T-r_e profiles is not observed in the negligible secondary droplet activation above cloud base (see very clean unimodal and clean unimodal cases), because very little to no aerosols are left available for nucleation even at the very large S values aloft. Since the updraft in the model is forced to a linear increase of 0.9 ms^{-1} km^{-1}, the cloud continues to grow vertically, leading to regrowth of r_e due to the ongoing coalescence of the remaining cloud droplets. As mentioned above, in nature, clouds with no new activation will rainout almost completely. They will reach very high S, but due to a lack of condensational heating, they will not develop any further. The practical impact of these results is to document the occurrence of secondary droplet activation well above the base of convective clouds with warm rain. The negative dr_e/dT in the modeled T-r_e profile indicates the secondary activation of aerosols that were not activated at cloud base and implies that the SAZ can be detected by remote sensing. Nevertheless, the appearance of SAZ in nature is not necessarily connected to inactivated Aitken mode particles. It could also be caused by the entrainment of aerosols of any size that can be activated even at S below S_{max}.

3.3. Detection of Microphysical Zones Based on Satellite T-r_e Profiles

There are unique relationships between the microphysical zones and their manifestation in the T-r_e profiles. Accordingly, satellite-retrieved T-r_e profiles can be used to infer microphysical zones, including the newly defined

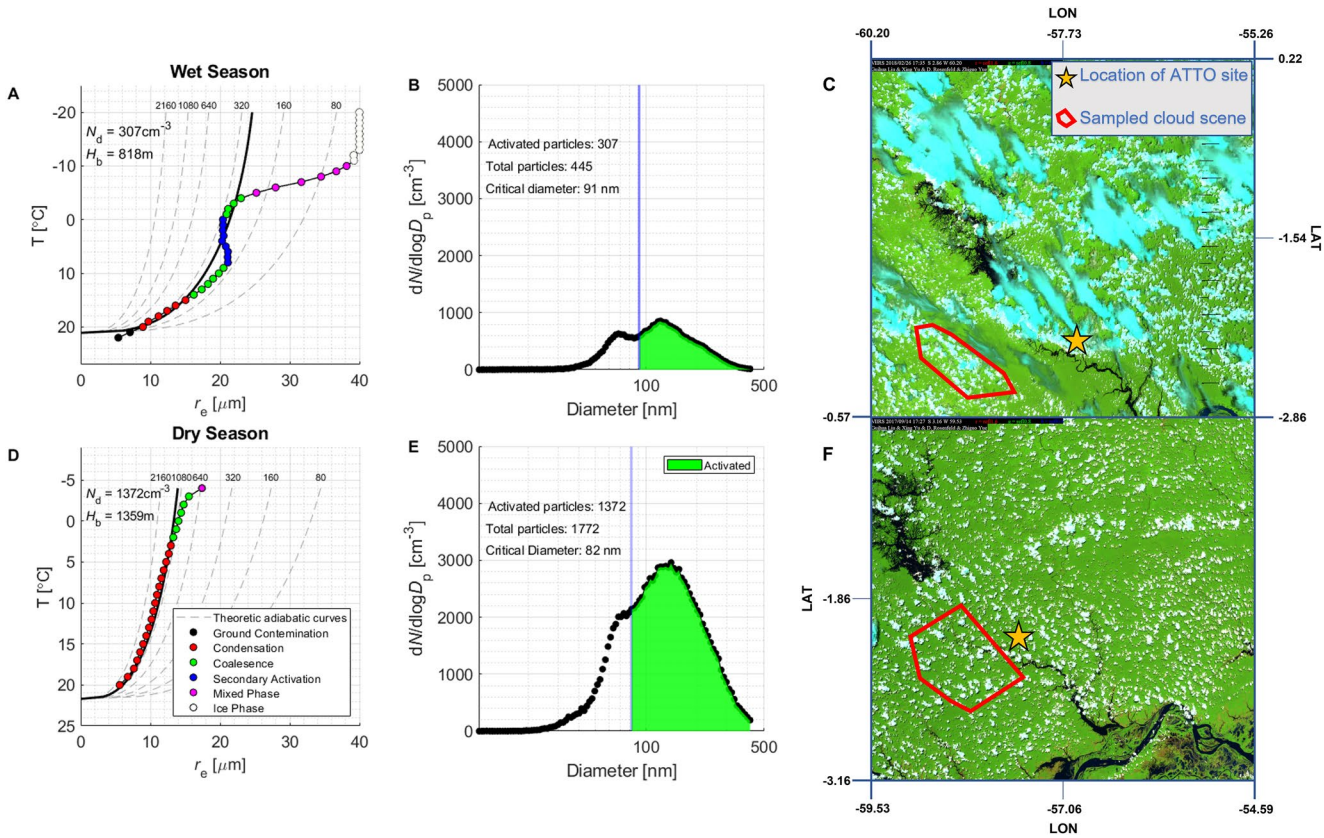

Figure 5. Satellite retrieved T-r_e profiles of exemplary cloud scenes during the Amazonian wet and dry seasons close to the ATTO region, color-coded by different microphysical zones (panels A and D); and the 1-hr average ASD before the satellite overpass of each case study as measured by the SMPS on the ATTO mast (Panels B and E). Panels C and F show the true-color satellite image of each case. The ATTO location is marked by a star and the sampled cloud scene by the red polygon.

SAZ. Two cloud scenes close to ATTO were used as case studies to investigate and demonstrate the applicability of satellite T-r_e profiles. Cloud scene A (red polygon in Figure 5a) is a cumulonimbus cloud that was taken within approximately 69 km from the ATTO site during the wet season (26 February 2018 at 17:22 UTC). This season is characterized by relatively low CCN concentrations (Pöhlker et al., 2016). The retrieved N_d is 307 cm^{-3} and cloud base height is 818 m, as estimated by the lifting condensation level. The first two points of this T-r_e profile are semi-transparent cloud pixels that might cause a distortion of the retrieval and are considered as ground contamination. The 1-hr average ASD before the satellite overpass (Figure 5b) clearly shows a Hoppel minimum at 88 nm. The number of activated particles at cloud base (Figure 5b) is equal to N_d. Accumulating the N_d largest particles on the ASD yields the smallest diameter to be activated, that is, the critical diameter. In this case the critical diameter is 91 nm. This result suggests that the activated particles at cloud base are accumulation mode particles down to that threshold. The SAZ is clearly identified above the coalescence zone at the 8°C isotherm. The activation of either remaining Aitken mode particles from cloud base and/or entrained aerosols at higher levels, causes a reduction of r_e with decreasing T. The new droplets are added to the preexisting large cloud drops undergoing coalescence, which leads to a renewed growth of r_e with decreasing T above the 0°C isotherm. This means that the coalescence microphysical zone is again dominant there. The rapid growth of r_e toward colder subzero temperatures can also be interpreted as a mixed phase of liquid and ice and eventually full glaciation of the cloud (Rosenfeld and Lensky, 1998). Cloud scene B (red polygon Figure 5d) is a cluster of cumulus congestus clouds that was taken within approximately 26 km from ATTO during the dry season (14 September 2017 at 17:27 UTC), which is characterized by relatively high concentrations of CCN (Pöhlker et al., 2016). The retrieved N_d for the dry season case is 1,372 cm^{-3} and the cloud base height is 1,359 m. The 1-hr average ASD (Figure 5e) of this case is unimodal with an inflection point instead of a clear Hoppel minimum. Thus, the separation of modes is less clear in comparison with Cloud scene A. Higher N_d at cloud base with smaller r_e (compared to Cloud scene A), decrease the condensational growth rate of droplets with decreasing T and strongly suppress the coalescence

processes, therefore a SAZ signature is not identified. At the 2°C isotherm, the r_e becomes sufficiently large for the coalescence process to dominate up to the cloud's top.

4. Discussion

The SAZ signature allows us to identify a significant occurrence of new droplets nucleation above the cloud base. The origins of the particles on which the new droplets are formed can either be Aitken mode particles that were not activated at cloud base or entrained particles of all size aloft. In the first case, S aloft has to exceed the S_{max} near cloud base. A stronger SAZ, which means lower $-dr_e/dT$, can imply an increased nucleation of smaller droplets, hence a greater latent heat release that increases the buoyancy. A deeper SAZ means that the top of the SAZ reaches lower temperatures. It can imply a deeper layer of aerosol activation above cloud base; thus the latent heat release occurs higher in the cloud. Increased buoyancy due to enhanced and/or higher occurrence of latent heat release leads to cloud invigoration. The invigoration of deep convective clouds may also lead to enhanced lightning activity (Thornton et al., 2017; Yuan et al., 2011).

As mentioned in Section 2.2, the parcel model is limited to cloud processes in the water phase only ($T > -10$°C). However, satellite retrieved cloud scenes can be more vertically developed than represented in the model, growing well above the −10°C isotherm (see Cloud scene A). The rapid growth of r_e above the subzero temperatures indicates a mixed phase of ice and water particles. At a maximum threshold r_e of 40 μm and/or temperatures colder than −38°C, the ice phase is dominant, and the cloud is considered fully glaciated (Rosenfeld and Lensky, 1998). As mentioned in Section 3.1, another limitation of the model compared to observations is manifested in the polluted case. For example, cloud scene B compared to the modeled polluted case: Both cases represent highly polluted situations with high CCN concentration at cloud base. The parcel model initiates coalescence and warm rain at the 5°C isotherm and later on allows secondary activation, even with the truncation of the larger particles. However, in nature this does not happen in such polluted situations. Andreae et al. (2004), Rosenfeld, Fischman, et al. (2014), Rosenfeld, Liu, et al. (2014) and Braga et al. (2017) showed in different aircraft campaigns in deep tropical convective clouds that, when the air is highly polluted, the coalescence zone is mostly delayed to the mixed-phase zone or suppressed altogether. As can be seen in Cloud scene B, the coalescence is much weaker and leads into the beginning of the mixed phased zone with no secondary activation. Whether the origins of the particles are from the cloud base or entrainment aloft, the SAZ described in this study requires a large S, which is caused by the preceding coalescence. With that being said, in some cases secondary nucleation of droplets might also occur before coalescence dominates, during the condensational growth of the cloud. It might happen either due to entrainment, or in highly polluted clouds that are updraft limited. In those clouds the S_{max} at the cloud base is rather small due to the activation of many particles. When the updraft increases with height to the extent that S exceeds the S_{max} at cloud base, a SAZ might occur even during the condensational growth phase. This type of SAZ differs from the SAZ discussed in this paper and will be addressed in a subsequent study.

Figure 6 shows the updated conceptual T-r_e model with the addition of the line of SAZ for clean and polluted clouds. The clean state (blue and cyan lines) is characterized by low aerosol concentration, thus the r_e increases rapidly above cloud base. The coalescence process is enhanced and leads to early warm rain. In the case where the cloud approaches supercooled temperatures and ice particles start to form, the observed r_e increases sharply with height until all droplets have frozen and r_e is stabilized. The cloud is then considered fully glaciated. The coalescence and rainout decrease the integrated surface area available for condensation, thus S increases. High S allows activation of additional cloud droplets if additional CCN are available, either from cloud base or entrained from aloft. In nature, clouds that undergo significant coalescence and/or warm rainout almost always experience SAZ (blue line). Otherwise, clouds would have difficulty developing further, due to the high S and a lack of sufficient condensational latent heating (cyan line).

In the polluted case (black line), there is a larger number of CCN at cloud base. That leads to a small rate of increase of r_e with height and suppression of the coalescence process. If the coalescence is suppressed up to the freezing level, rainout and SAZ will not appear on the T-r_e profile.

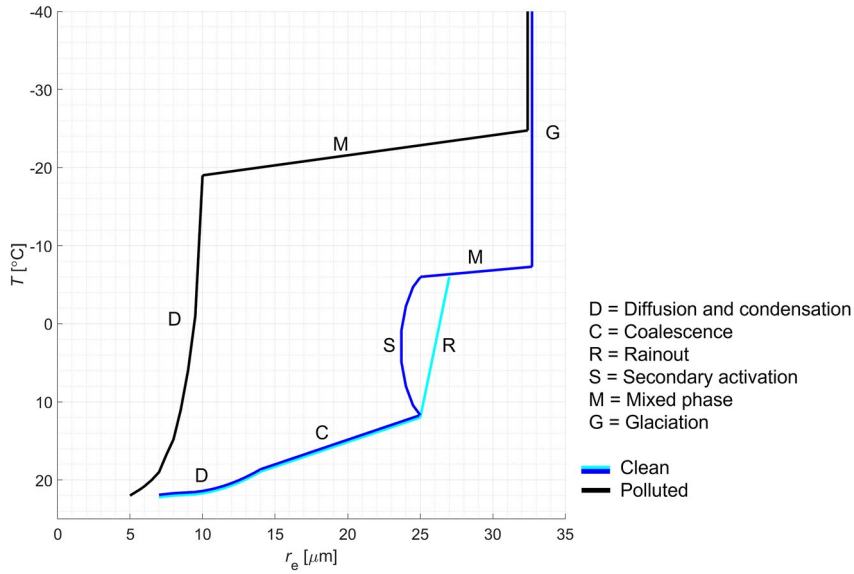

Figure 6. An updated conceptual diagram of the microphysical zones for clean and polluted clouds based on the vertical evolution of the T-r_e relationships including the secondary activation of droplets above cloud base. The clean cloud (blue and cyan lines) has low N_d and large r_e at cloud base. The enhanced coalescence leads to early warm rain. When the cloud reaches the subzero temperatures and start to glaciate, r_e is increased sharply with height. The coalescence and rainout decrease the integrated surface area available for condensation. The increased S allows activation of additional available CCN into cloud droplets. In nature, clouds with significant coalescence and/or warm rainout usually experience SAZ (blue line). Otherwise, clouds would have difficulty developing further, because of the high S and a lack of sufficient condensational latent heating (cyan line). The polluted case (black line) is characterized by larger N_d and a smaller r_e at cloud base. Suppression of the coalescence process occurs. If the suppression is all the way up to the freezing level, rainout and SAZ will not appear on the T-r_e profile.

5. Summary

A method to identify the occurrence of secondary activation of droplets above deep convective cloud bases by satellite measurements was introduced in this paper. The earlier T-r_e conceptual model by Rosenfeld and Lensky (1998) assumes CCN activation into cloud droplets at cloud base. Thus, a stabilization or moderation of r_e after exceeding a threshold of approximately 14 μm with decreasing T was considered as resulting from rainout of the larger drops from the cloud. However, considering additional nucleation of droplets above cloud base, in the present study the moderation or inversion of dr_e/dT is ascribed to the existence of a significant secondary drop activation zone (SAZ). When pronounced coalescence and warm rain forming processes dominate during the cloud vertical growth, the droplets' integrated surface area is reduced. The reduction of the water surface area available for condensation decreases the condensation rate and increases the supersaturation to high values beyond the maximum supersaturation at cloud base. As a result, particles within the cloud parcel that could not be activated at cloud base due to their lower critical supersaturation are activated aloft. If the rate of large drops elimination is lower than the rate of new droplets activation, there is a decrease of r_e with decreasing T and increasing height. The origins of the newly activated particles can be either UAP from the cloud base and/or entrained particles aloft from the boundaries of the clouds.

The method presented in this study is an updated version of the previous conceptual T-r_e model. The detection of SAZ signature on a T-r_e profile, is introduced here for the first time. This conceptual model was demonstrated with adiabatic parcel model simulations for different scenarios of aerosol concentrations and size distributions. The SAZ signature was also observed in satellite-retrieved T-r_e profiles. The possibility to apply this methodology to satellite retrieved T-r_e profiles allows a detailed analysis of cloud microphysics in large areas and over long periods of time. This will increase the understanding of cloud-aerosol interactions at the micro and macro scale. The occurrence of the SAZ signature has climatic importance in shaping cloud microstructure aloft and a possible propagation to cloud radiative forcing.

Disclaimer

This paper contains results of research conducted under the Technical/Scientific Cooperation Agreement between the National Institute for Amazonian Research, the State University of Amazonas, and the Max-Planck-Gesellschaft e.V.; the opinions expressed are the entire responsibility of the authors and not of the participating institutions.

Conflict of Interest

The authors declare no conflicts of interest relevant to this study.

Data Availability Statement

The satellite data of the case studies presented in this study is available on the VIIRS data set found at the NOAA's Comprehensive Large Array-data Stewardship System (2022; https://www.avl.class.noaa.gov/). The ATTO data used in this study are available via the ATTO data portal through https://www.attoproject.org/. The output data from the IDL program of the sampled cloud scenes have been deposited in supplementary data files for use in follow-up studies (Efraim et al., 2022; https://doi.org/10.5061/dryad.h44j0zpnr). For data requests beyond the available data, please refer to the corresponding author.

Acknowledgments
The authors acknowledge the support by the Instituto Nacional de Pesquisas da Amazônia (INPA). The authors would like to thank all people involved in the technical, logistical, and scientific support within the ATTO project. The authors acknowledge the Meteorological Institute of Shaanxi Province, China, for the IDL program for retrieving the cloud microphysical parameters from NPP/VIIRS. For the operation of the ATTO site, we acknowledge the support by the Max Planck Society (MPG), the German Federal Ministry of Education and Research (BMBF contracts 01LB1001A, 01LK1602B, and 01LK2101B) and the Brazilian Ministério da Ciência, Tecnologia e Inovação (MCTI/FINEP contract 01.11.01248.00) as well as the Amazon State University (UEA), FAPEAM, LBA/INPA and SDS/CEUC/RDS-Uatumã. This work has been funded by the Max Planck Society (MPG) and FAPESP - Fundação de Amparo à Pesquisa do Estado de São Paulo, Grant No. 2017/17047-0. Marco A. Franco acknowledges the financial support of CNPq for the Ph.D. scholarship, project number 169842/2017-7, CAPES, for a sandwich doctorate at the Max Planck Institute for Chemistry, project number 88887.368025/2019-00, and FAPESP, Grant No. 2021/13610-8. Leslie A. Kremper acknowledges the financial support by the Max Planck Graduate Center with the Johannes-Gutenberg University, Mainz. In addition, this study was partially supported by the BSF Grant No. 2020809.

References

Andreae, M. O., Acevedo, O. C., Araùjo, A., Artaxo, P., Barbosa, C. G. G., Barbosa, H. M. J., et al. (2015). The Amazon Tall Tower Observatory (ATTO): Overview of pilot measurements on ecosystem ecology, meteorology, trace gases, and aerosols. *Atmospheric Chemistry and Physics*, *15*(18), 10723–10776. https://doi.org/10.5194/acp-15-10723-2015

Andreae, M. O., Rosenfeld, D., Artaxo, P., Costa, A. A., Frank, G. P., Longo, K. M., & Silva-Dias, M. A. F. (2004). Smoking rain clouds over the Amazon. *Science*, *303*(5662), 1337–1342. https://doi.org/10.1126/science.1092779

Arakawa, A., & Schubert, W. H. (1974). Interaction of a cumulus cloud ensemble with the large-scale environment, part I. *Journal of the Atmospheric Sciences*, *31*(3), 674–701. https://doi.org/10.1175/1520-0469(1974)031<0674:ioacce>2.0.co;2

Artaxo, P., Rizzo, L. V., Brito, J. F., Barbosa, H. M. J., Arana, A., Sena, E. T., et al. (2013). Atmospheric aerosols in Amazonia and land use change: From natural biogenic to biomass burning conditions. *Faraday Discussions*, *165*, 203. https://doi.org/10.1039/c3fd00052d

ATTO - Amazon Tall Tower Observatory. (2020). *ATTO - Amazon tall tower observatory*. Retrieved from https://www.attoproject.org/

Bera, S., Chowdhuri, S., & Prabha, T. V. (2022). A new methodology for the statistical descriptions of particle-by-particle measurements of liquid droplets in cumulus clouds. *Quarterly Journal of the Royal Meteorological Society*, *148*(743), 842–859. https://doi.org/10.1002/qj.4234

Bott, A. (1997). An efficient numerical flux method for the solution of the stochastic collection equation. *Journal of Aerosol Science*, *28*, S745–S746. https://doi.org/10.1016/s0021-8502(97)85371-2

Braga, R. C., Rosenfeld, D., Krüger, O. O., Ervens, B., Holanda, B. A., Wendisch, M., et al. (2021). Linear relationship between effective radius and precipitation water content near the top of convective clouds: Measurement results from ACRIDICON–CHUVA campaign. *Atmospheric Chemistry and Physics*, *21*(18), 14079–14088. https://doi.org/10.5194/acp-21-14079-2021

Braga, R. C., Rosenfeld, D., Weigel, R., Jurkat, T., Andreae, M. O., Wendisch, M., et al. (2017). Further evidence for CCN aerosol concentrations determining the height of warm rain and ice initiation in convective clouds over the Amazon basin. *Atmospheric Chemistry and Physics*, *17*(23), 14433–14456. https://doi.org/10.5194/acp-17-14433-2017

Bréon, F. M., Tanré, D., & Generoso, S. (2002). Aerosol effect on cloud droplet size monitored from satellite. *Science*, *295*(5556), 834–838. https://doi.org/10.1126/science.1066434

Cotton, W. R., Bryan, G., & van den Heever, S. C. (2011). The mesoscale structure of extratropical cyclones and middle and high clouds. *International Geophysics*, *99*, 527–672. https://doi.org/10.1016/s0074-6142(10)09916-x

Efraim, A., Oliver, L., Daniel, R., Ramon, B., Marco, F., Leslie, K., et al. (2022). Satellite processed data [Dataset]. Dryad. https://doi.org/10.5061/dryad.h44j0zpnr

Fan, J., Leung, L. R., Rosenfeld, D., Chen, Q., Li, Z., Zhang, J., & Yan, H. (2013). Microphysical effects determine macrophysical response for aerosol impacts on deep convective clouds. *Proceedings of the National Academy of Sciences*, *110*(48), E4581–E4590. https://doi.org/10.1073/pnas.1316830110

Fan, J., Rosenfeld, D., Zhang, Y., Giangrande, S. E., Li, Z., Machado, L. A. T., et al. (2018). Substantial convection and precipitation enhancements by ultrafineaerosol particles. *Science*, *359*(6374), 411–418. https://doi.org/10.1126/science.aan8461

Feingold, G., Remer, L. A., Ramaprasad, J., & Kaufman, Y. J. (2001). Analysis of smoke impact on clouds in Brazilian biomass burning regions: An extension of Twomey's approach. *Journal of Geophysical Research*, *106*(D19), 22907–22922. https://doi.org/10.1029/2001jd000732

Franco, M. A., Ditas, F., Kremper, L. A., Machado, L. A. T., Andreae, M. O., Araújo, A., et al. (2022). Occurrence and growth of sub-50 nm aerosol particles in the Amazonian boundary layer. *Atmospheric Chemistry and Physics*, *22*(5), 3469–3492. https://doi.org/10.5194/acp-22-3469-2022

Freud, E., & Rosenfeld, D. (2012). Linear relation between convective cloud drop number concentration and depth for rain initiation: Drop concentration and rain initiation. *Journal of Geophysical Research*, *117*(D2). https://doi.org/10.1029/2011JD016457

Freud, E., Rosenfeld, D., Andreae, M. O., Costa, A. A., & Artaxo, P. (2008). Robust relations between CCN and the vertical evolution of cloud drop size distribution in deep convective clouds. *Atmospheric Chemistry and Physics*, *8*(6), 1661–1675. https://doi.org/10.5194/acp-8-1661-2008

Freud, E., Rosenfeld, D., & Kulkarni, J. R. (2011). Resolving both entrainment-mixing and number of activated CCN in deep convective clouds. *Atmospheric Chemistry and Physics*, *11*(24), 12887–12900. https://doi.org/10.5194/acp-11-12887-2011

Grosvenor, D. P., Sourdeval, O., Zuidema, P., Ackerman, A., Alexandrov, M. D., Bennartz, R., et al. (2018). Remote sensing of droplet number concentration in warm clouds: A review of the current state of knowledge and perspectives. *Reviews of Geophysics*, *56*(2), 409–453. https://doi.org/10.1029/2017rg000593

Gunn, R., & Phillips, B. B. (1957). An experimental investigation of the effect of air pollution on the initiation of rain. *Journal of the Atmospheric Sciences*, *14*(3), 272–280. https://doi.org/10.1175/1520-0469(1957)014<0272:aeiote>2.0.co;2

Hoppel, W. A., & Frick, G. M. (1986). Ion-Aerosol attachment coefficients and the steady-state charge distribution on aerosols in a bipolar ion environment. *Aerosol Science and Technology*, *5*(1), 1–21. https://doi.org/10.1080/02786828608959073

Huang, T., Zhu, Y., Rosenfeld, D., Yang, Y., Lam, D. H. Y., Leung, W. H., et al. (2022). Regime-dependent impacts of aerosol particles and updrafts on the cloud condensation nuclei and the enhanced warm rain suppression: Evidence from synergistic satellite and LiDAR observations. *Geophysical Research Letters*, *49*(3). e2021GL097315. https://doi.org/10.1029/2021gl097315

Hudson, J. G., Noble, S., & Tabor, S. (2015). Cloud supersaturations from CCN spectra Hoppel m*inima. Journal of Geophysical Research: Atmospheres*, *120*(8), 3436–3452. https://doi.org/10.1002/2014jd022669

IPCC. (2013). Summary for Policymakers. In *Climate Change 2013: The Physical Science Basis* (pp. 1–30). Contribution of Working Group I to the Fifth Assessment report of the Intergovernmental Panel on Climate Change [T. F., Stocker, D., Qin, G.-K., Plattner, M., Tignor, S. K., Allen, J. , Boschung, et al. (Eds.)]. Cambridge University Press, Cambridge, United Kingdom and New York, NY, USA. https://doi.org/10.1017/CBO9781107415324.004

IPCC. (2021). Summary for policymakers. In *Climate change 2021: The physical science basis* (pp. 3–32). Contribution of Working Group I to the Sixth Assessment Report of the Intergovernmental Panel on Climate Change [V., MassonDelmotte, P., Zhai, A., Pirani, S. L., Connors, C., Péan, S., Berger, N., Caud, Y., Chen, L., Goldfarb, M. I., Gomis, M., Huang, K., Leitzell, E., Lonnoy, J. B. R., Matthews, et al. (Eds.)]. Cambridge University Press, Cambridge, United Kingdom and New York, NY, USA. https://doi.org/10.1017/9781009157896.001

Khain, A. P., Phillips, V., Benmoshe, N., & Pokrovsky, A. (2012). The role of small soluble aerosols in the microphysics of deep maritime clouds. *Journal of the Atmospheric Sciences*, *69*(9), 2787–2807. https://doi.org/10.1175/2011jas3649.1

Konwar, M., Maheskumar, R. S., Kulkarni, J. R., Freud, E., Goswami, B. N., & Rosenfeld, D. (2012). Aerosol control on depth of warm rain in convective clouds: Aerosol control on depth of warm rain. *Journal of Geophysical Research*, *117*(D13). https://doi.org/10.1029/2012jd017585

Lensky, I. M., & Rosenfeld, D. (2006). The time-space exchangeability of satellite retrieved relations between cloud top temperature and particle effective radius. *Atmospheric Chemistry and Physics*, *6*(10), 2887–2894. https://doi.org/10.5194/acp-6-2887-2006

Moran-Zuloaga, D., Ditas, F., Walter, D., Saturno, J., Brito, J., Carbone, S., et al. (2018). Long-term study on coarse mode aerosols in the Amazon rain forest with the frequent intrusion of Saharan dust plumes. *Atmospheric Chemistry and Physics*, *18*(13), 10055–10088. https://doi.org/10.5194/acp-18-10055-2018

Nakajima, T., Higurashi, A., Kawamoto, K., & Penner, J. E. (2001). A possible correlation between satellite-derived cloud and aerosol microphysical parameters. *Geophysical Research Letters*, *28*(7), 1171–1174. https://doi.org/10.1029/2000gl012186

NOAANOAANOAA's Comprehensive Large Array-data Steward*ship Sy*stem. (2022). Noa*a.Gov. Retrieved from https://www.avl.class.noaa.gov/saa/products/search?sub_id=0&datatype_family=VIIRS_SDR&submit.x=22&submit.y=4*

Paluch, I. R., & Baumgardner, D. G. (1989). Entrainment and fine-scale mixing in a continental convective cloud. *Journal of the Atmospheric Sciences*, *46*(2), 261–278. https://doi.org/10.1175/1520-0469(1989)046<0261:eafsmi>2.0.co;2

Paluch, I. R., & Knight, C. A. (1984). Mixing and the evolution of cloud droplet size spectra in a vigorous continental cumulus. *Journal of the Atmospheric Sciences*, *41*(11), 1801–1815. https://doi.org/10.1175/1520-0469(1984)041<1801:mateoc>2.0.co;2

Pan, Z., Rosenfeld, D., Zhu, Y., Mao, F., Gong, W., Zang, L., & Lu, X. (2021). Observational quantification of aerosol invigoration for deep convective cloud lifecycle properties based on geostationary satellite. *Journal of Geophysical Research: Atmospheres*, *126*(9). e2020JD034275. https://doi.org/10.1029/2020jd034275

Pinsky, M., Khain, A., Mazin, I., & Korolev, A. (2012). Analytical estimation of droplet concentration at cloud base: Droplet concentration at cloud base. *Journal of Geophysical Research: Atmospheres*, *117*(D18), https://doi.org/10.1029/2012jd017753

Pinsky, M., Khain, A., & Shapiro, M. (2001). Collision efficiency of drops in a wide range of Reynolds numbers: Effects of pressure on spectrum evolution. *Journal of the Atmospheric Sciences*, *58*(7), 742–764. https://doi.org/10.1175/1520-0469(2001)058<0742:ceodia>2.0.co;2

Pinsky, M. B., & Khain, A. P. (2002). Effects of in-cloud nucleation and turbulence on droplet spectrum formation in cumulus clouds. *Quarterly Journal of the Royal Meteorological Society*, *128*(580), 501–533. https://doi.org/10.1256/003590002321042072

Pöhlker, C., Walter, D., Paulsen, H., Könemann, T., Rodríguez-Caballero, E., Moran-Zuloaga, D., et al. (2019). Land cover and its transformation in the backward trajectory footprint region of the Amazon Tall Tower Observatory. *Atmospheric Chemistry and Physics*, *19*(13), 8425–8470. https://doi.org/10.5194/acp-19-8425-2019

Pöhlker, M. L., Ditas, F., Saturno, J., Klimach, T., Hrabě de Angelis, I., Araùjo, A. C., et al. (2018). Long-term observations of cloud condensation nuclei over the Amazon rain forest – Part 2: Variability and characteristics of biomass burning, long-range transport, and pristine rain forest aerosols. *Atmospheric Chemistry and Physics*, *18*(14), 10289–10331. https://doi.org/10.5194/acp-18-10289-2018

Pöhlker, M. L., Pöhlker, C., Ditas, F., Klimach, T., Hrabe de Angelis, I., Araújo, A., et al. (2016). Long-term observations of cloud condensation nuclei in the Amazon rain forest – Part 1: Aerosol size distribution, hygroscopicity, and new model parametrizations for CCN prediction. *Atmospheric Chemistry and Physics*, *16*(24), 15709–15740. https://doi.org/10.5194/acp-16-15709-2016

Pöhlker, M. L., Zhang, M., Campos Braga, R., Krüger, O. O., Pöschl, U., & Ervens, B. (2021). Aitken mode particles as CCN in aerosol- and updraft-sensitive regimes of cloud droplet formation. *Atmospheric Chemistry and Physics*, *21*(15), 11723–11740. https://doi.org/10.5194/acp-21-11723-2021

Prabha, T. V., Khain, A., Maheshkumar, R. S., Pandithurai, G., Kulkarni, J. R., Konwar, M., & Goswami, B. N. (2011). Microphysics of premonsoon and monsoon clouds as seen from in situ measurements during the cloud aerosol interaction and precipitation enhancement experiment (CAIPEEX). *Journal of the Atmospheric Sciences*, *68*(9), 1882–1901. https://doi.org/10.1175/2011jas3707.1

Quaas, J., Ming, Y., Menon, S., Takemura, T., Wang, M., Penner, J. E., et al. (2009). Aerosol indirect effects – General circulation model intercomparison and evaluation with satellite data. *Atmospheric Chemistry and Physics*, *9*(22), 8697–8717. https://doi.org/10.5194/acp-9-8697-2009

Rosenfeld, D. (2007). New insights to cloud seeding for enhancing precipitation and for hail suppression. *Journal of Weather Modification*, *39*, 61–69. https://doi.org/10.1007/978-1-4020-5835-6_6

Rosenfeld, D. (2018). Cloud-aerosol-precipitation interactions based of satellite retrieved vertical profiles of cloud microstructure. In *Remote sensing of aerosols, clouds, and precipitation* (pp. 129–152). https://doi.org/10.1016/b978-0-12-810437-8.00006-2

Rosenfeld, D., Fischman, B., Zheng, Y., Goren, T., & Giguzin, D. (2014). Combined satellite and radar retrievals of drop concentration and CCN at convective cloud base: Rosenfeld et al.; retrieving convective cloud base CCN. *Geophysical Research Letters*, *41*(9), 3259–3265. https://doi.org/10.1002/2014gl059453

Rosenfeld, D., Kaufman, Y. J., & Koren, I. (2006). Switching cloud cover and dynamical regimes from open to closed Benard cells in response to the suppression of precipitation by aerosols. *Atmospheric Chemistry and Physics*, *6*(9), 2503–2511. https://doi.org/10.5194/acp-6-2503-2006

Rosenfeld, D., & Lensky, I. M. (1998). Satellite-based insights into precipitation formation processes in continental and maritime convective clouds. *Bulletin of the American Meteorological Society*, *79*(11), 2457–2476. https://doi.org/10.1175/1520-0477(1998)079<2457:sbiipf>2.0.co;2

Rosenfeld, D., Liu, G., Yu, X., Zhu, Y., Dai, J., Xu, X., & Yue, Z. (2014). High-resolution (375 m) cloud microstructure as seen from the NPP/VIIRS satellite imager. *Atmospheric Chemistry and Physics*, *14*(5), 2479–2496. https://doi.org/10.5194/acp-14-2479-2014

Rosenfeld, D., Lohmann, U., Raga, G. B., O'Dowd, C. D., Kulmala, M., Fuzzi, S., et al. (2008). Flood or drought: How do aerosols affect precipitation? *Science*, *321*(5894), 1309–1313. https://doi.org/10.1126/science.1160606

Rosenfeld, D., Woodley, W. L., Lerner, A., Kelman, G., & Lindsey, D. T. (2008). Satellite detection of severe convective storms by their retrieved vertical profiles of cloud particle effective radius and thermodynamic phase. *Journal of Geophysical Research*, *113*(D4), D04208. https://doi.org/10.1029/2007jd008600

Rosenfeld, D., Zheng, Y., Hashimshoni, E., Pöhlker, M. L., Jefferson, A., Pöhlker, C., et al. (2016). Satellite retrieval of cloud condensation nuclei concentrations by using clouds as CCN chambers. *Proceedings of the National Academy of Sciences*, *113*(21), 5828–5834. https://doi.org/10.1073/pnas.1514044113

Seinfeld, J. H., & Pandis, S. N. (1998). *Atmospheric chemistry and physics: From air pollution to climate change*. Wiley.

Shinozuka, Y., Clarke, A. D., Nenes, A., Jefferson, A., Wood, R., McNaughton, C. S., et al. (2015). The relationship between cloud condensation nuclei (CCN) concentration and light extinction of dried particles: Indications of underlying aerosol processes and implications for satellite-based CCN estimates. *Atmospheric Chemistry and Physics*, *15*(13), 7585–7604. https://doi.org/10.5194/acp-15-7585-2015

Slingo, A., & Slingo, J. M. (1988). The response of a general circulation model to cloud longwave radiative forcing. I: Introduction and initial experiments. *Quarterly Journal of the Royal Meteorological Society*, *114*(482), 1027–1062. https://doi.org/10.1002/qj.49711448209

Squires, P. (1958). The microstructure and colloidal stability of warm clouds. *Tellus*, *10*(2), 256–261. https://doi.org/10.1111/j.2153-3490.1958.tb02011.x

Thornton, J. A., Virts, K. S., Holzworth, R. H., & Mitchell, T. P. (2017). Lightning enhancement over major oceanic shipping lanes. *Geophysical Research Letters*, *44*(17), 9102–9111. https://doi.org/10.1002/2017gl074982

Twomey, S. (1977). The influence of pollution on the shortwave albedo of clouds. *Journal of the Atmospheric Sciences*, *34*(7), 1149–1152. https://doi.org/10.1175/1520-0469(1977)034<1149:tiopot>2.0.co;2

Warner, J. (1969). The microstructure of cumulus cloud. Part I. General features of the droplet spectrum. *Journal of the Atmospheric Sciences*, *26*(5), 1049–1059. https://doi.org/10.1175/1520-0469(1969)026<1049:tmoccp>2.0.co;2

Wendisch, M., Pöschl, U., Andreae, M. O., Machado, L. A. T., Albrecht, R., Schlager, H., et al. (2016). Acridicon–Chuva campaign: Studying tropical deep convective clouds and precipitation over Amazonia using the new German research aircraft Halo. *Bulletin of the American Meteorological Society*, *97*(10), 1885–1908. https://doi.org/10.1175/bams-d-14-00255.1

Yuan, T., Remer, L. A., Pickering, K. E., & Yu, H. (2011). Observational evidence of aerosol enhancement of lightning activity and convective invigoration: Aerosol enhancement of lightning. *Geophysical Research Letters*, *38*(4), https://doi.org/10.1029/2010gl046052

Zheng, Y., & Rosenfeld, D. (2015). Linear relation between convective cloud base height and updrafts and application to satellite retrievals: Satellite retrieval of cloud updrafts. *Geophysical Research Letters*, *42*(15), 6485–6491. https://doi.org/10.1002/2015gl064809

Zhu, Y., Rosenfeld, D., Yu, X., Liu, G., Dai, J., & Xu, X. (2014). Satellite retrieval of convective cloud base temperature based on the NPP/VIIRS imager. *Geophysical Research Letters*, *41*(4), 1308–1313. https://doi.org/10.1002/2013gl058970